INTERNATIONAL JOURNAL FOR NUMERICAL METHODS IN FLUIDS, VOL. 6, 789–809 (1986)

A NUMERICAL METHOD FOR THE CALCULATION OF INCOMPRESSIBLE, STEADY, SEPARATED FLOWS AROUND AEROFOILS

G. TZABIRAS*

Department of Naval Architecture and Marine Engineering, National Technical University of Athens, Athens 10682, Greece

A. DIMAS†

Department of Ocean Engineering, M.I.T., U.S.A.

AND

T. LOUKAKIS‡

Department of Naval Architecture and Marine Engineering, National Technical University of Athens, Athens 10682, Greece

SUMMARY

The present work deals with the numerical calculation of the incompressible turbulent flow around aerofoils. An orthogonal curvilinear grid of 'C' type is used for the solution of the time averaged equations and Reynolds stresses are modelled according to the k–ε turbulence model. PISO and SIMPLE algorithms are used to solve the strongly coupled system of the derived finite volume equations and convergence is improved by applying the method of variable local underrelaxation factors. Comparisons between the calculated and measured pressure distributions are presented for NACA 0012 and NACA 4412 wing sections. The formation of separation bubbles according to calculations is also shown.

KEY WORDS Conformal Mapping Reynolds Equations Separated Flows

INTRODUCTION

The calculation of steady, separated flows around aerofoils is always important for many applications in fluid mechanics such as the design of wings, propeller blades, wind generators, cascades and other engineering configurations. In this case the presence of recirculation zones introduces two further difficulties in the computations. First, a very fine discretization of the flow field is necessary and, secondly, the appropriate modelling of the Reynolds stresses, which appear in the momentum equations of the mean flow, has not yet been established.

For the computations around an aerofoil we are mainly interested in flows with restricted recirculation areas, whereas in other cases (for example the flow over a backward-facing step) they extend to large regions of the calculation domain. These areas may exist for angles of attack smaller than the stall angle, which corresponds to the maximum lift. For higher angles of attack massive separation is often related to unsteady flow phenomena characterized by vortex shedding.

So far several methods have been developed[1,2] and satisfactory results have been obtained for

*Lecturer
†Graduate Student
‡Professor

0271–2091/86/110789–21$10.50

Received 10 October 1985
Revised 8 April 1986

the solution of the Navier–Stokes equations in the case of separated laminar flows past aerofoils. Successful attempts have also been made for tubulent attached flows,[3] where the Reynolds stresses can be modelled by simple eddy viscocity models. On the contrary, these models are not valid for turbulent separated flows where at least two-equation models are needed to overcome the closure problem. A remarkable preliminary investigation into this problem using a two-equation turbulence model (k–ε) has been reported by Rhie and Chow.[4] For the solution of the differential equations they used a co-ordinate transformation of the initial non-orthogonal grid around the aerofoil to a Cartesian system. Results have been presented for 0012 and 4412 NACA sections.

The purpose of this work is to present a finite volume method for the solution of the complete Reynolds equations in a surface-orientated co-ordinate system, which can be dependent on the angle of incidence. The Reynolds stresses are modelled by the standard k–ε turbulence model.[5] Although the introduction of an isotropic eddy viscocity is questionable, applications of this model have shown[6] that satisfactory predictions for the mean flow components can be obtained. The flow field around the aerofoil is considered as fully turbulent because the location of transition cannot be predicted analytically. However if this location is known both laminar and turbulent regions can be treated simultaneously.

In several previous investigations[7,8] it has been shown that the errors which are introduced by the application of a certain discretization scheme are often of the same importance as those introduced by the turbulence model. In order to diminish the numerical diffusion in the present method, an orthogonal curvilinear co-ordinate system is used and the governing equations are solved in the physical plane. This co-ordinate system is also beneficial for both the application of the boundary conditions and the convergence of the resulting algebraic equations.

CO-ORDINATE SYSTEM

In the present work a 'C' type orthogonal curvilinear co-ordinate system is used for the computation of the turbulent flow field around an aerofoil. The corresponding numerical grid is generated by a conformal mapping technique which is described in the sequel.

The selection of this co-ordinate system is suggested by the finite difference formulation of the initial transport equations which govern the particular flow field. There are at least two regions of the flow around an aerofoil where the co-ordinate lines have to be orientated with the mean velocity vector in order to diminish the discretization errors due to 'false'[7,9] diffusion. The first is the region around the leading edge, where the flow is highly accelerated and large pressure gradients occur. The second is the trailing edge region where there is a strong interaction with the near wake and recirculation zones appear at large angles of attack. For both regions the above 'C' type co-ordinate system is aligned with the flow direction near the solid boundary and allows for any desired grid refinement, depending on the available computer.

The above considerations explain also why we have abandoned the adoption of two other familiar orthogonal curvilinear co-ordinate systems which can be used. The one is related to a grid generated by the intersections of stream and potential lines all around the foil. The refinement of this grid near the leading edge stagnation point is essentially difficult. Moreover serious numerical diffusion errors may be introduced since the accurate location of the stagnation point is not known *a priori*. The other co-ordinate system corresponds to an 'O' type grid around the aerofoil, which presents difficulties for the computation of the flow near the trailing edge.[10]

The transformation

The orthogonal curvilinear grid around a foil is generated by a direct conformal mapping of the

foil onto a circle. The mapping function has the general from[11]

$$\zeta = C_{-1}\frac{z}{R_P} + C_0 + \sum_{n=1}^{\infty} C_n \frac{R_P^n}{z^n}, \tag{1}$$

where $\zeta = x + iy$ is the plane of the foil (Figure 1), $z = Re^{i\varphi}$ is the plane of the circle with radius R_P and $C_n = A_n + iB_n$, $n = -1, 0, 1, 2\ldots$ are the coefficients of the transformation.

For the foil contour one can easily obtain the relations

$$x(\varphi) = A_{-1}\cos\varphi - B_{-1}\sin\varphi + A_0 + \sum_{n=1}^{\infty}[A_n\cos n\varphi + B_n\sin n\varphi],$$

$$y(\varphi) = B_{-1}\cos\varphi + A_{-1}\sin\varphi + B_0 + \sum_{n=1}^{\infty}[B_n\cos n\varphi - A_n\sin n\varphi]. \tag{2}$$

If the co-ordinates x, y are known functions of the angle φ on the circle of radius R_P then the transformation coefficients are calculated from (2) by the following integrals:

$$A_0 = \frac{1}{2\pi}\int_0^{2\pi} x(\varphi)\,d\varphi, \qquad B_0 = \frac{1}{2\pi}\int_0^{2\pi} y(\varphi)\,d\varphi,$$

$$A_{-1} - A_1 = \frac{1}{\pi}\int_0^{2\pi} y(\varphi)\sin\varphi\,d\varphi, \qquad B_1 + B_{-1} = \frac{1}{\pi}\int_0^{2\pi} y(\varphi)\cos\varphi\,d\varphi, \tag{3}$$

$$A_{-1} + A_1 = \frac{1}{\pi}\int_0^{2\pi} x(\varphi)\cos\varphi\,d\varphi, \qquad B_1 - B_{-1} = \frac{1}{\pi}\int_0^{2\pi} x(\varphi)\sin\varphi\,d\varphi,$$

$$A_n = -\frac{1}{\pi}\int_0^{2\pi} y(\varphi)\sin n\varphi\,d\varphi, \qquad B_n = \frac{1}{\pi}\int_0^{2\pi} y(\varphi)\cos n\varphi\,d\varphi, \quad n \geqslant 2.$$

However, for an arbitrary foil the functions $x(\varphi)$ and $y(\varphi)$ are not specified. To overcome this difficulty we apply an iterative procedure for the determination of coefficients A_n and B_n, which follows the following steps:

1. For a given set of co-ordinates (x_P, y_P) on the foil contour (Figure 1) the coefficients A_n, B_n, $n = -1, \ldots, N$ are calculated approximately by the thin wing transformation method of Brockett.[11]
2. For the calculated values of A_n, B_n the angles φ_P which correspond to the co-ordinates (x_P, y_P) are estimated on the circle plane. For a point (x_P, y_P) the corresponding angle φ_P is estimated by finding the minimum of the squared distance

$$E_i = [x_P - x(\varphi_i)]^2 + [y_P - y(\varphi_i)]^2,$$

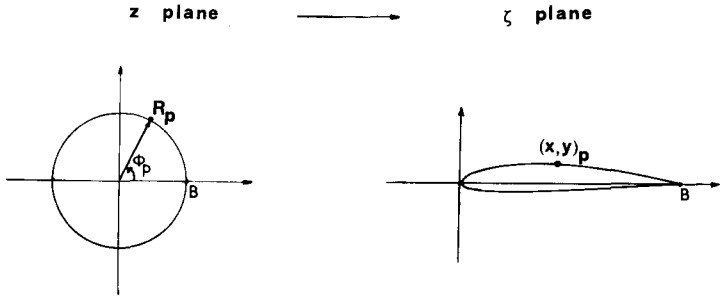

Figure 1. The conformal transformation

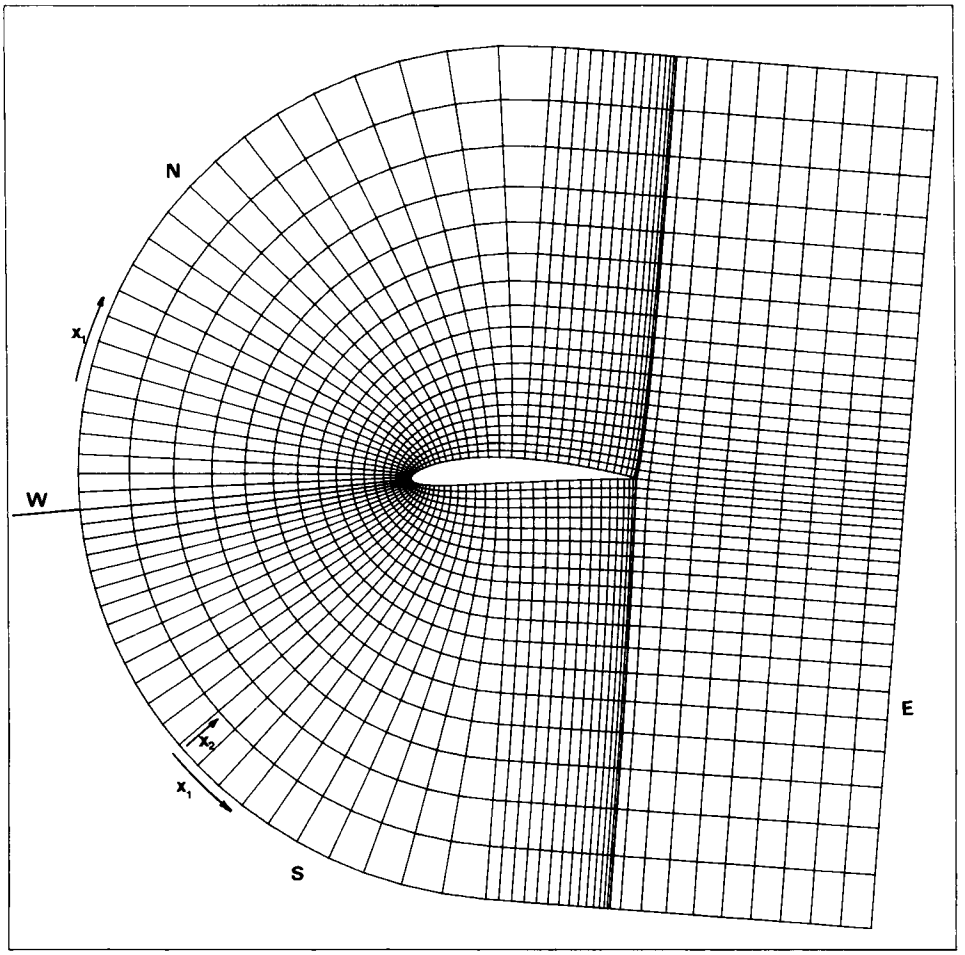

Figure 2. The orthogonal curvilinear grid around the NACA 4412 aerofoil

where $[\varphi_i]$ is a specified partition on the circle and $x(\varphi_i)$, $y(\varphi_i)$ are calculated from (2). The partition $[\varphi_i]$ is selected so that the error in the calculation of φ_P is always below 0·01°.

3. Given the set (x_P, y_P) and the corresponding angles φ_P, the coefficients A_n and B_n are calculated from integrals (3) by numerical integration. For an accurate evaluation of these integrals the functions $x(\varphi)$ and $y(\varphi)$ are assumed to vary linearly between two adjacent points on the foil.
4. Steps 2 and 3 are repeated until A_n, B_n and φ_P are convergent within specified error bounds. Usually 30 iterations are needed for this convergence.
5. Steps 2 to 4 are repeated by increasing the number N of coefficients A_n, B_n until the maximum error in the calculation of x_P and y_P from relations (2) is below 0·1 per cent.

For the typical NACA sections which have been tested so far, it was found that a number N equal to 18 is adequate for an accurate representation of the wing section.

Grid generation

After the coefficients of the general transformation (1) have been calculated, the orthogonal curvilinear grid around the aerofoil can be created by the mapping of a coresponding grid on the circle plane.[12]

A typical orthogonal curvilinear grid around the NACA 4412 wing section is shown in Figure 2. For computational purposes we define four boundaries around this 'C' type grid, that is the south (S) and north (N) boundaries which are separated by the common west boundary (W), and the east (E) boundary, which is also refered as the exist boundary.

For the numerical solution of the Reynolds equations around the aerofoil we define two sets of co-ordinate lines along the two grid dimensions. These are the constant x_2 lines which are parallel to the foil contour and have their origin on the west boundary, and orthogonal to them, the constant x_1 lines. The mean velocity components are defined as u_1 along the lines $x_2 = \text{constant}$ and u_2 along $x_1 = \text{constant}$ (Figure 2).

THE GOVERNING EQUATIONS

In the orthogonal curvilinear system around the aerofoil the general transport equation for a scalar variable Φ can be written as

$$C(\Phi) = D(\Phi) + S_\Phi, \tag{4}$$

where Φ stands for the mean velocity components (u_1, u_2), the turbulence kinetic energy k and its dissipation rate ε. The term $C(\Phi)$ describes the convection terms of the variable Φ, i.e.

$$C(\Phi) = \frac{1}{h_1 h_2}\left[\frac{\partial}{\partial x_1}(\rho u_1 h_2 \Phi) + \frac{\partial}{\partial x_2}(\rho u_2 h_1 \Phi)\right],$$

where h_1 and h_2 are the metrics along the $x_2 = \text{constant}$ and $x_1 = \text{constant}$ lines, respectively. The term $D(\Phi)$ in equation (4) shows the diffusion terms of the variable Φ, i.e.

$$D(\Phi) = \frac{1}{h_2 h_2}\left[\frac{\partial}{\partial x_1}\left(\Gamma_\Phi \frac{h_2}{h_1}\frac{\partial \Phi}{\partial x_1}\right) + \frac{\partial}{\partial x_2}\left(\Gamma_\Phi \frac{h_1}{h_2}\frac{\partial \Phi}{\partial x_2}\right)\right],$$

where Γ_Φ is given in Table I together with the expressions for S_Φ for each variable Φ and the constants of the k–ε model of turbulence. The components of the stress tensor σ_{ij} which appear in the source terms S_φ of Table I are expressed as follows

$$\sigma_{ij} = \mu_e\left[\frac{h_j}{h_i}\frac{\partial}{\partial x_i}\left(\frac{u_j}{h_j}\right) + \frac{h_i}{h_j}\frac{\partial}{\partial x_j}\left(\frac{u_i}{h_i}\right)\right], \quad \sigma_{ii} = 2\mu_e\left[\frac{1}{h_i}\frac{\partial u_i}{\partial x_i} + \frac{u_j}{h_i h_j}\frac{\partial h_i}{\partial x_j}\right],$$

where, under the assumption of an isotropic eddy viscosity μ_t, the effective viscosity μ_e is given by

$$\mu_e = \mu + \mu_t = \mu + C_D \rho k^2/\varepsilon. \tag{5}$$

Finally, the term G contained in the k and ε source terms is defined as

$$G = \frac{1}{2\mu_t}[\sigma_{11}^2 + \sigma_{22}^2 + 2\sigma_{12}^2].$$

The derivation of the above set of equations may be found in several References,[13,14] and it can be shown that it is identical with the one used by Hackman, Raithby and Strong[7] for the calculation of the flow over a backward-facing step.

The selected conformal mapping satisfies the requirement of continuity of curvatures along the

Table I. Source terms and constants for momentum and k–ε equations

Φ	Γ_Φ	S_Φ
u_i	μ_e	$-\frac{1}{h_i}\frac{\partial p}{\partial x_i}-\frac{\rho u_i u_j}{h_i h_j}\frac{\partial h_i}{\partial x_j}+\frac{\rho u_j^2}{h_i h_j}\frac{\partial h_j}{\partial x_i}$
$i=1,2$		$+\frac{1}{h_i h_j}\left[\frac{\partial}{\partial x_i}(h_j\sigma_{ii})+\frac{\partial}{\partial x_j}(h_i\sigma_{ij})\right]$
		$+\frac{\sigma_{ij}}{h_i h_j}\frac{\partial h_i}{\partial x_j}-\frac{\sigma_{jj}}{h_i h_j}\frac{\partial h_j}{\partial x_i}-D(\Phi_i)$
		$j=2$ if $i=1$
		$j=1$ if $i=2$
k	$\frac{\mu_t}{\sigma_k}$	$G-\rho\varepsilon$
ε	$\frac{\mu_t}{\sigma_\varepsilon}$	$C_1 G\frac{\varepsilon}{k}-C_2\rho\frac{\varepsilon^2}{k}$

$C_1 = 1{\cdot}44$, $C_2 = 1{\cdot}92$, $C_D = 0{\cdot}09$, $\sigma_k = 1$, $\sigma_\varepsilon = 1{\cdot}3$

co-ordinate lines, which is implied by the curvature terms $(1/h_i h_j)\partial h_j/\partial x_i$ of the transport equations.

THE SOLUTION METHOD

A finite volume approach[8] is used for the numerical solution of the set of transport equations (4). The control volumes for each variable Φ are shown in Figure 3 and they correspond to the staggered grid of Patankar and Spalding.[15] Integration of equation (4) in the corresponding control volume of a variable Φ results in an algebraic equation of the form

$$A_P\Phi_P = A_N\Phi_N + A_S\Phi_S + A_E\Phi_E + A_W\Phi_W + S_\Phi, \tag{6}$$

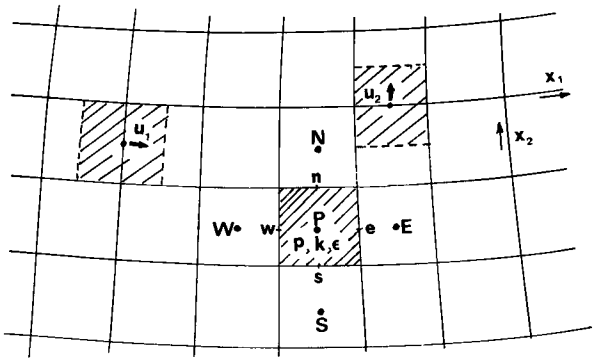

Figure 3. The control volumes

where $\Phi = u_1, u_2, k, \varepsilon$ and the subscripts P,N,S,E,W correspond to the grid points shown in Figure 3.

The convection and diffusion terms of the initial equation (4) are approximated according to the hybrid scheme of Spalding,[16] that is central differencing is used when $|Pe| < 2$ and upwind differencing when $|Pe| \geqslant 2$, where Pe is the local Peclet number. The coefficients A in equations (6) are generally functions of the unknown variables Φ and therefore an iterative procedure has to be applied for the solution of these equations.

Boundary conditions

Equations (6) are of elliptic type for each variable Φ and boundary conditions need to be specified all around the external boundary of the 'C' type grid and on the aerofoil surface.

At S and N boundaries (Figure 2) the mean velocity components u_1 and u_2 are calculated as components of the undisturbed velocity at infinity U_∞ and k, ε are taken equal to zero. This assumption is valid only when the boundaries are located far enough from the foil surface, at a distance which depends on both the Reynolds number and the angle of attack and can be estimated only by numerical experiments. So far, this distance has been found to be equal to three chord lengths for flows without separation and three to five chord lengths for flows with separation. An alternative was used for small angles of attack where the velocity components at boundaries S and N were calculated from the potential flow solution according to the conformal transformation.[12] This improved the numerical results since the external boundary could be placed closer to the foil surface for a given number of grid nodes.

At the exit boundary, E, fully developed conditions are applied for all variables Φ, which corresponds to a Neumann condition with $A_E = 0$. In all the tested cases this boundary was located about one chord length downstream from the trailing edge.

On the foil surface the standard wall function method[5] is used for the velocity component u_1, the turbulence kinetic energy k and its dissipation rate ε. The near wall nodes are assumed to lie in the logarithmic law region where the flow is assumed one dimensional and the velocity is given by relation

$$U_1^+ = \frac{1}{\kappa} \ln(Ey^+), \tag{7}$$

where

$$y^+ = \frac{y}{\nu}\left(\frac{\tau_w}{\rho}\right)^{1/2},$$

$$U_1^+ = u_1\left(\frac{\tau_w}{\rho}\right)^{-1/2},$$

$$\kappa \approx 0{\cdot}42,$$

$$E \approx 9{\cdot}79,$$

τ_w is the wall shear stress, ν is the fluid kinematic viscosity, ρ is the fluid density and y is the normal distance from the wall.

In the same region the generation of k is almost equal to its dissipation rate[17] and after some manipulations the following expressions can be derived:

$$\tau_w = \frac{\rho C_D^{1/4} \kappa k^{1/2}}{\ln(Ey^+)} u_1,$$
$$y^+ = \frac{C_D^{1/4} k^{1/2}}{\nu} y, \tag{8}$$
$$\varepsilon = \frac{C_D^{3/4} k^{3/2}}{\kappa y}.$$

These expressions are introduced in equations (6) as the boundary conditions on the wall. The u_2 velocity component is equal to zero on the same boundary, whereas for the pressure correction equation (which is described in the next section) the Neumann condition $\partial p'/\partial y = 0$ is applied.

The solution algorithm

Since the momentum equations for components u_1 and u_2 contain unknown pressure gradients, a simultaneous solution for the pressure field is needed. In the present work we follow the procedures of the SIMPLE[15] and the PISO[18] algorithms which are based on a pressure correction equation derived for the satisfaction of mass conservation. According to these algorithms the following steps are followed:

1. An initial pressure field is guessed according to the potential flow solution around the aerofoil.
2. The systems of u_1 and u_2 momentum equations (6) are solved (generally these systems are solved by successive applications of the tridiagonal matrix algorithm[19]).
3. The calculated velocities u_1 and u_2 are corrected in order to satisfy the continuity equation in the control volumes of the pressure. Equations (6) can be written in the form

$$u_{1P} = \sum_i A_i u_{1i} + Du_1(P_e - P_w) + S'_{u_1},$$
$$u_{2P} = \sum_i A'_i u_{2i} + Du_2(P_n - P_s) + S'_{u_2}, \qquad i = N, S, E, W. \tag{9}$$

Assuming that the coefficients A_i and A'_i and the source terms of the discretized equations (9) are constant, the following velocity perturbation equations can be derived[18] corresponding to the points e, w, n and s of the pressure control volume (Figure 3):

$$\delta u_{1_e} = \sum_i A_{ie} \delta u_{1_{ie}} + Du_{1_e}(p'_E - p'_P),$$
$$\delta u_{1_w} = \sum_i A_{iw} \delta u_{1_{iw}} + Du_{1_w}(p'_P - p'_W), \tag{10}$$
$$\delta u_{2_n} = \sum_i A_{in} \delta u_{2_{in}} + Du_{2_n}(p'_N - p'_P),$$
$$\delta u_{2_s} = \sum_i A_{is} \delta u_{2_{is}} + Du_{2_s}(p'_P - p'_S),$$

where p' stands for the correction of the pressure field and the index i corresponds to the four neighbouring points of e, w, n or s, as in equation (9). If the above velocity perturbations are inserted as the velocity corrections in the integral form of the continuity equation for each pressure control volume, a system of algebraic equations of the general form (6) is derived with the pressure correction p' as unknown variable. This system can be written in the form

$$[A][p'] = -[D^*] + [F]. \tag{11}$$

In equation (11) the elements of $[A]$ are directly proportional to the coefficients of the pressure gradient terms of equations (10), $[D^*]$ stands for the divergence of the velocity field in the pressure control volumes and the elements of $[F]$ are linear combinations of the summation terms on the right hand sides of equations (10). A direct solution of (11) would be very difficult since the elements of $[F]$ are functions of the unknown pressure corrections. This is why simplified forms of equations (11) are used in order to calculate the velocity and pressure corrections.

In the SIMPLE algorithm the elements of the matrix $[F]$ are assumed equal to zero, that is all the terms under the summation sign are neglected in equations (10) and the velocity perturbations are directly related to the pressure perturbations. Then the system (11) can be easily solved (as for the momentum equations) to obtain an approximate pressure correction field which is used to update the pressure field. The velocity components are corrected correspondingly using the truncated form of equations (10).

With the PISO algorithm the pressure correction field is estimated in two steps. In the first step the same procedure as in the SIMPLE algorithm is followed, that is $[F]$ is neglected and a first approximation of p' is calculated, which is used to obtain the velocity perturbations. In the second step these velocity perturbations are used to evaluate the elements of $[F]$. Then the system (11) is solved again and a new pressure correction field is obtained. This second step is expected to give a better approximation for the pressure field, as it corresponds to a more accurate formulation of the pressure correction equation.

4. The obtained velocity components u_1 and u_2 are used for the solution of k and ε equations. Then the values of the effective viscosity μ_e are updated from (5).
5. Steps 2 to 4 are repeated until numerical convergence is achieved. For the momentum equations numerical convergence is obtained when the following relation is satisfied:

$$\sum_{\mathrm{P}} |\mathrm{Res}_{\mathrm{P}}^{i}| < c,$$

where $\mathrm{Res}_{\mathrm{P}}^{i}$ is the residual source equal to the difference between the two sides of equation (11) for node P during the ith iteration, that is

$$\mathrm{Res}_{\mathrm{P}}^{i} = A_{\mathrm{P}}\Phi_{\mathrm{P}} - (A_{\mathrm{N}}\Phi_{\mathrm{N}} + A_{\mathrm{S}}\Phi_{\mathrm{S}} + A_{\mathrm{E}}\Phi_{\mathrm{E}} + A_{\mathrm{W}}\Phi_{\mathrm{W}} + S_{\Phi}), \tag{12}$$

and c is defined as

$$c = (2Y_{\mathrm{w}}U_{\infty}^{2})b,$$

where Y_{w} is the distance of the external node from the foil surface on the west boundary (Figure 2) and b is a constant which is specified according to the desired convergence accuracy. (Usually the sum of the residual sources is normalized by the term in parentheses so that convergence is directly related to b). For all tested cases the value of b was equal to 10^{-4}, corresponding to a maximum change in the velocity field below 0·01 per cent during the last iterations of the numerical solution.

For the pressure field, convergence is obtained when the sum of the velocity divergence in all control volumes of the pressure is less than a constant c' which is equal to c/U_{∞}.

Improvement of convergence rate

Owing to the elliptic, non-linear and strongly implicit character of the system of equations (6), an underrelaxation method has to be applied in order to obtain convergence.[18] According to this method the updated value Φ_{new} of a variable Φ is estimated as a linear combination of its previous value Φ_{old} and the corresponding solution Φ_0 of system (6), that is

$$\Phi_{new} = r\Phi_0 + (1-r)\Phi_{old}, \quad 0 < r < 1,$$

where r is the underrelaxation factor. If this factor is assumed constant for a certain transport equation, two serious disadvantages arise. First, the value of the underrelaxation factor for which convergence is obtained is not known *a priori* and numerical tests are necessary for its specification. Secondly, the convergence rate is often very slow because it has been shown numerically that as the solution proceeds higher underrelaxation factors can be advantageous.

In order to overcome the above disadvantages Neuberger *et al.*[20] have developed a method for an analytical determination of the local underrelaxation factors. This method is based on the analogy between the solution of the unsteady-state equations and the iterative solution of the steady-state equations. It has been shown[20] that a time-dependent method with an allowable time step Δt^i corresponds to an iterative steady-state method with local underrelaxation factors

$$r_P^i = \frac{Q_P^i \Delta t^i}{1 + Q_P^i \Delta t^i}, \quad Q_P^i = \frac{A_P^i}{\rho V_P}, \tag{13}$$

where r_P^i is the local underrelaxation factor for grid point P during the ith iteration, A_P^i is the coefficient of Φ_P in equation (6) and V_P is the control volume of the corresponding variable. The allowable time step Δt^i can be estimated by the conditions to be fulfilled, so that the time-dependent solution is stable and convergent. The general unsteady transport equation can be written as

$$\rho \frac{\partial \Phi}{\partial t} = D(\Phi) - C(\Phi) + S_\Phi, \tag{14}$$

where the diffusion, convection and source terms have the same expressions as in equation (4). Convergence of the discretized equation (14) for grid point P at the ith time step is obtained when the following condition is fulfilled:

$$\left| \frac{\partial f(t_i, \Phi_P)}{\partial \Phi_P} \right| \Delta t_i \leqslant \kappa, \tag{15}$$

where κ depends on the special problem under consideration and

$$f(t, \Phi_P) = \frac{\partial \Phi_P}{\partial t}. \tag{16}$$

Experience has shown that κ is in the range $0{\cdot}1 \leqslant \kappa \leqslant 1$. In the present work the lower value of κ, equal to 0·1, has been used in all tested cases.

Comparison of (14) with the discretized steady-state equation (6) and the residual source expression (12) results in relation

$$-\rho V_P \frac{\partial \Phi_P}{\partial t} = \mathrm{Res}_P^i. \tag{17}$$

Using this relation, condition (15) can be transformed to the following inequality:

$$\Delta t^i \leqslant \kappa \frac{|\mathrm{Res}_P^i|}{|\bar{V}\nabla \cdot \mathrm{Res}_P^i|} \tag{18}$$

where $\bar{V}$ is the velocity vector at grid point P. The above relation determines the allowable time step as a function of the residual sources of the steady-state solution and therefore an optimum underrelaxation factor r_P^i through (13).

Table II. The convergence behaviour of the numerical solution

	Normalized residual source sums with constant underrelaxation factors equal to 0·5			Normalized residual source sums with optimum local underrelaxation factors		
Iteration	u_1 momentum	u_2 momentum	velocity divergence	u_1 momentum	u_2 momentum	velocity divergence
1	1·31	2·05	2·66	1·31	2·16	4·37
20	$3{\cdot}09 \times 10^{-1}$	$1{\cdot}92 \times 10^{-1}$	$8{\cdot}46 \times 10^{-2}$	$2{\cdot}91 \times 10^{-1}$	$2{\cdot}55 \times 10^{-1}$	$4{\cdot}14 \times 10^{-1}$
40	$2{\cdot}69 \times 10^{-1}$	$1{\cdot}54 \times 10^{-1}$	$2{\cdot}57 \times 10^{-2}$	$2{\cdot}91 \times 10^{-1}$	$2{\cdot}80 \times 10^{-1}$	$4{\cdot}66 \times 10^{-1}$
60	$2{\cdot}42 \times 10^{-1}$	$1{\cdot}70 \times 10^{-1}$	$2{\cdot}86 \times 10^{-2}$	$3{\cdot}31 \times 10^{-1}$	$3{\cdot}01 \times 10^{-1}$	$6{\cdot}93 \times 10^{-1}$
80	$2{\cdot}84 \times 10^{-1}$	$1{\cdot}76 \times 10^{-1}$	$3{\cdot}45 \times 10^{-2}$	$9{\cdot}48 \times 10^{-2}$	$5{\cdot}21 \times 10^{-2}$	$7{\cdot}97 \times 10^{-2}$
100	$2{\cdot}88 \times 10^{-1}$	$2{\cdot}50 \times 10^{-1}$	$6{\cdot}55 \times 10^{-2}$	$1{\cdot}80 \times 10^{-1}$	$1{\cdot}17 \times 10^{-1}$	$1{\cdot}79 \times 10^{-1}$
120	$2{\cdot}50 \times 10^{-1}$	$1{\cdot}49 \times 10^{-1}$	$2{\cdot}52 \times 10^{-2}$	$8{\cdot}29 \times 10^{-2}$	$8{\cdot}10 \times 10^{-2}$	$9{\cdot}72 \times 10^{-2}$
140	$1{\cdot}09 \times 10^{-1}$	$5{\cdot}17 \times 10^{-2}$	$9{\cdot}11 \times 10^{-3}$	$2{\cdot}57 \times 10^{-2}$	$2{\cdot}46 \times 10^{-2}$	$2{\cdot}84 \times 10^{-2}$
160	$6{\cdot}55 \times 10^{-2}$	$7{\cdot}30 \times 10^{-2}$	$4{\cdot}76 \times 10^{-3}$	$7{\cdot}33 \times 10^{-3}$	$5{\cdot}57 \times 10^{-3}$	$7{\cdot}14 \times 10^{-3}$
180	$3{\cdot}60 \times 10^{-2}$	$3{\cdot}93 \times 10^{-2}$	$2{\cdot}63 \times 10^{-3}$	$2{\cdot}50 \times 10^{-3}$	$2{\cdot}12 \times 10^{-3}$	$2{\cdot}49 \times 10^{-3}$
200	$1{\cdot}74 \times 10^{-2}$	$1{\cdot}76 \times 10^{-2}$	$1{\cdot}30 \times 10^{-3}$	$9{\cdot}50 \times 10^{-4}$	$7{\cdot}19 \times 10^{-4}$	$9{\cdot}98 \times 10^{-4}$
220	$8{\cdot}38 \times 10^{-3}$	$8{\cdot}80 \times 10^{-3}$	$6{\cdot}48 \times 10^{-4}$			
240	$4{\cdot}45 \times 10^{-3}$	$4{\cdot}56 \times 10^{-3}$	$3{\cdot}46 \times 10^{-4}$			
260	$2{\cdot}62 \times 10^{-3}$	$2{\cdot}49 \times 10^{-3}$	$2{\cdot}09 \times 10^{-4}$			
280	$1{\cdot}49 \times 10^{-3}$	$1{\cdot}46 \times 10^{-3}$	$1{\cdot}33 \times 10^{-4}$			
300	$9{\cdot}75 \times 10^{-4}$	$9{\cdot}73 \times 10^{-4}$	$9{\cdot}11 \times 10^{-5}$			

NACA 0012: $Re = 3 \times 10^6$; angle of attack 14°, grid nodes 40 × 20

By applying the above procedure for the determination of the local underrelaxation factors in each transport equation, a serious improvement in the convergence rate was achieved. A typical example of the solution behaviour with the number of iterations is given in Table II where the two methods of constant and variable local underrelaxation factors are compared. The corresponding computations have been carried out for the NACA 0012 wing section at an angle of attack equal to 14°. The numerical grid had 40 × 20 nodes and the Reynolds number was equal to 3×10^6. With constant underrelaxation factors equal to 0·5 for all variables, convergence was obtained in 300 iterations, as the values of the normalized residual sums in Table II show. When the method of the variable underrelaxation factors was used, convergence was achieved in 200 iterations. It is also remarkable that with this method the normalized residual sums have higher values during the first iterations, whereas they are reduced drastically as the solution proceeds.

Numerical experiments have shown that increasing the number of grid nodes in order to obtain grid-independent solutions, the method of the variable underrelaxation factors required less than half the iterations which were necessary for convergence when constant underrelaxation factors were used. It should be noted here that the application of relation (13) has given convergent solutions only with the PISO algorithm. On the other hand, it has been found that when the constant underrelaxation factor method is applied both the SIMPLE and PISO algorithms require almost the same number of iterations to obtain convergence.

RESULTS

In order to test the accuracy and the behaviour of the present numerical method, computations have been carried out for NACA 0012 and NACA 4412 wing sections. In this section the results of the calculated surface pressure coefficients and corresponding lift coefficients are compared to

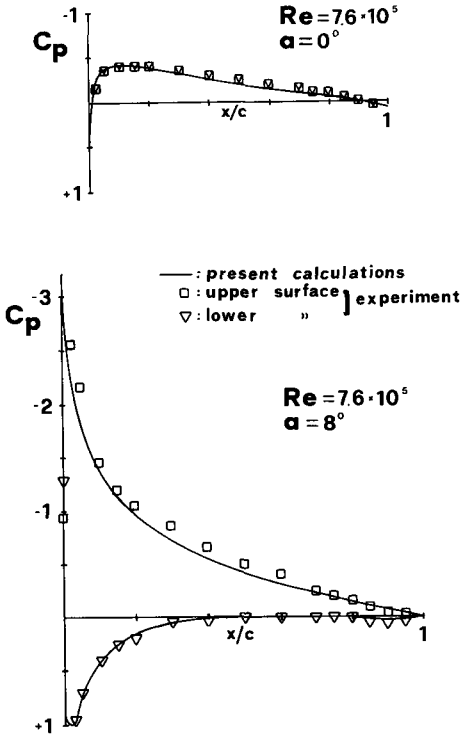

Figure 4. Comparison of pressure distributions around the NACA 0012 aerofoil

experiments. Also, the prediction of separation bubbles for high angles of attack is shown.

A PRIME 450 mini-computer was used for all computations. In some cases the computer configuration did not allow us to obtain grid-independent solutions and the finer grid used for the computations was 70 × 60 nodes (the first number corresponds to x_1 = constant lines and the second number to x_2 = constant lines).

NACA 0012 aerofoil

For NACA 0012 five different flow cases were tested, corresponding to angles of attack equal to 0°, 8°, 12°, 14° and 20°. In all cases the Reynolds number was 7·6 × 10^5, for which experimental data have been reported by Michos et al.[21]

0° angle of attack. Calculations have been performed for the zero angle of attack in order to check the symmetry of the numerical solution. A 50 × 60 grid was used with 80 nodes on the aerofoil surface and 150 iterations were needed for convergence, with the optimum underrelaxation factor method. When the underrelaxation factors were assumed constant and equal to 0·5, convergence was achieved in 290 iterations. Comparisons of calculated pressure coefficients C_P with experiments are shown in Figure 4 and good agreement is observed.

8° angle of attack. A 50 × 60 grid was again used and convergence was obtained in 160 iterations. The external boundaries N and S were placed at distances equal to three chord lengths from the aerofoil surface. Comparisons of calculated C_P with experimental values show (Figure 4) a

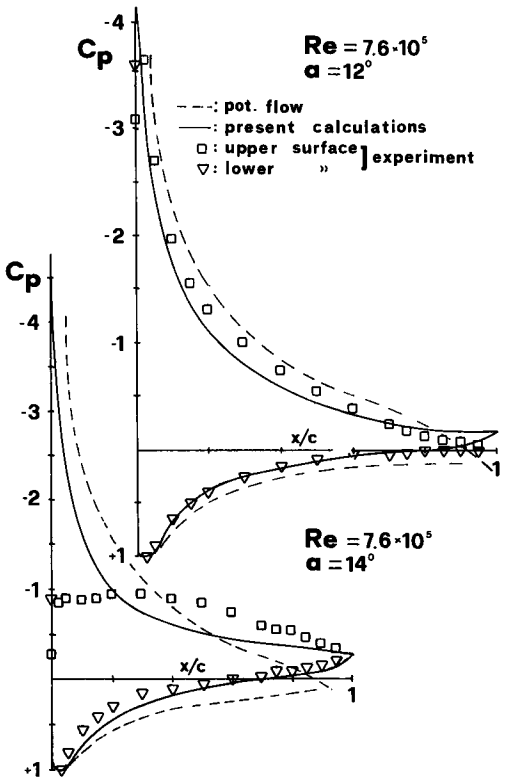

Figure 5. Comparison of pressure distributions around the NACA 0012 aerofoil

good agreement. The calculated lift coefficient C_L is 0·78, whereas the measured value was 0·82.

12° angle of attack. At this angle the flow is still attached. A 60 × 60 grid was used for the computations with 90 points on the aerofoil surface and convergence was achieved in 330 iterations (always with the optimum underrelaxation factor method). The N and S boundaries were located four chord lengths away from the aerofoil surface. Comparisons of calculated C_P with experiments are presented in Figure 5 and seem satisfactory. The measured C_L was 1·08 and according to calculations a value of 1·02 was obtained. In the same Figure the dashed line shows the potential flow calculations obtained by the conformal mapping method. In general the potential flow solution predicts higher values of C_P towards the leading edge, whereas large discrepancies are observed near the trailing edge between the predicted and the experimental values. As a result the calculated lift coefficient is always higher than that predicted by the turbulent flow solution. For this angle of attack the value of C_L calculated by the potential flow solution was 1·44.

14° angle of attack. Experiments showed that maximum lift was obtained between 13° and 14° angles of attack. At 14° unsteady flow phenomena were observed which cannot be predicted by the present method. However an attempt was made to calculate the steady flow field around the aerofoil by using the same grid as in the case of 12° incidence. Convergence was achieved in 450 iterations. In Figure 6 the scaled mean velocity vector field around the aerofoil is plotted and a separation bubble is observed starting at the point S, which lies almost at the middle of the chord. In Figure 5 comparisons of calculated to measured values of C_P are presented and large

discrepancies are observed on the upper surface of the aerofoil. The experimental pressure distribution on this surface implies an extended separation region where there is no negative peak in C_P (or at least it was too difficult to be measured). The calculated C_L is 1·09, whereas the measured value was 0·83 for 14° incidence and 1·11 for 13° incidence. This implies that near the stall angle and before unsteady separation occurs the present calculations adequately predict the lift coefficient.

At the same angle of attack calculations were carried out for a Reynolds number $Re = 6 \times 10^6$. The corresponding stall angle in this Reynolds number is about 16°.[22] Convergence was again obtained in 430 iterations. In Figure 7 the plotting of the mean velocity vectors shows the effect of the higher Reynolds number on the formation of the separation bubble. The separation point is located closer to the trailing edge, whereas the reattachment point is almost the same as in the previous case. The experimental[23] value of C_L is 1·40, whereas the calculated value was 1·15. When a 70 × 60 grid with 110 nodes on the aerofoil was used the latter value was improved significantly to 1·25. Unfortunately no grid-independent solution was obtained because of the limited computer configuration.

20° angle of attack. Calculations at this angle of attack were carried out in order to test the convergence behaviour of the present method. A 70 × 60 grid was used with 110 points on the aerofoil and the N and S boundaries were located at a distance of seven chord lengths from the aerofoil surface. Convergence was obtained in 700 iterations. In Figure 8 the calculated C_P is compared with experiments. Although surprisingly good agreement is observed, future applications of the method will demonstrate if it is reliable for flows at higher than stall angles of attack. In Figure 9 the plotting of the corresponding mean velocity vectors shows a large separation bubble extending almost all over the upper surface of the aerofoil. As a consequence, the calculated pressure coefficient on this area has almost a constant value except at a narrow region near the leading edge where high negative values are observed. The potential C_P values (dashed line in Figure 8) are quite different and show a remarkable difference in the location of the stagnation point. This is a well-known[11] difficiency of the potential flow methods.

NACA 4412 aerofoil

For the NACA 4412 aerofoil, calculations were carried out for two angles of attack, that is for 6·4° incidence at a Reynolds number $Re = 3 \times 10^6$ and for 13·87° incidence at $Re = 1{\cdot}5 \times 10^6$, for which experimental data exist.

6·4° angle of attack. A 50 × 60 grid was used in this case with 80 points on the aerofoil surface. Convergence was achieved in 170 iterations (with constant underrelaxation factors equal to 0·5, 380 iterations were needed for convergence). The external boundaries were placed at a distance of three chord lengths from the profile surface. In Figure 10 the calculated C_P is compared to experiments[22] and very good agreement is observed. The predicted C_L is 1·07, whereas its experimental value was 1·025.

13·87° angle of attack. This is the stall angle for a Reynolds number equal to $1{\cdot}5 \times 10^6$ according to experiments of Coles and Wadcock.[24] A 70 × 60 grid was used with 110 points on the aerofoil and the external boundaries were located at four chord lengths away from the foil surface. Convergence was achieved in 300 iterations. In Figure 10 comparisons are presented between the calculated and experimental C_P. Some discrepancies are observed on the upper surface of the profile where lower negative values of C_P are predicted, corresponding to a calculated lift coefficient

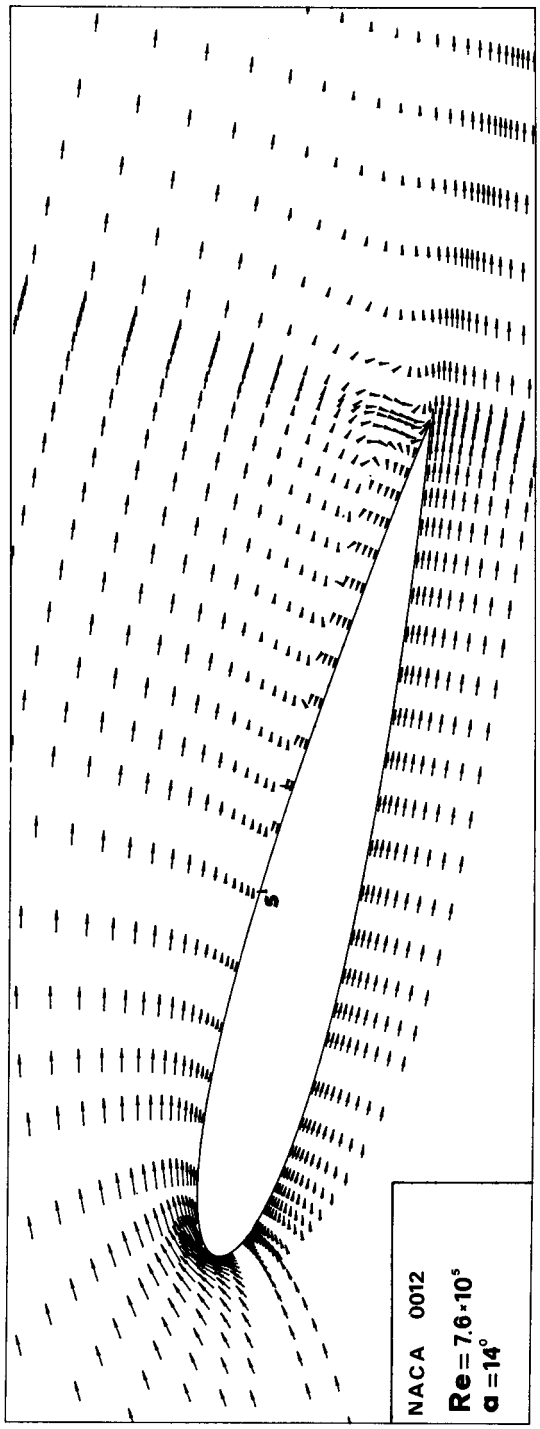

Figure 6. Mean velocity vector plot around the NACA 0012 aerofoil

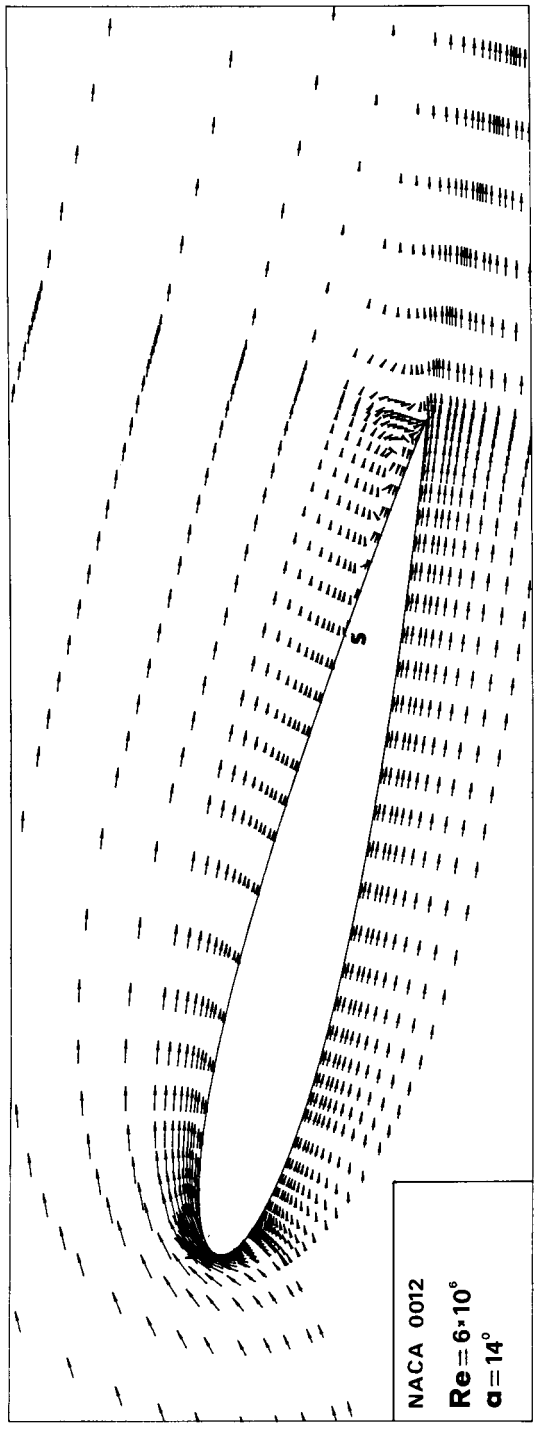

Figure 7. Mean velocity vector plot around the NACA 0012 aerofoil

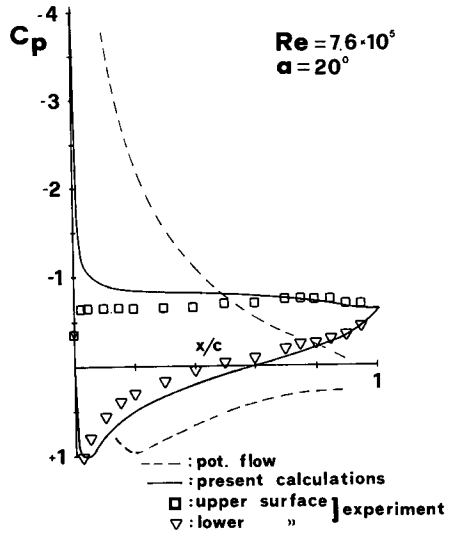

Figure 8. Comparison of pressure distributions around the NACA 0012 aerofoil

somewhat lower than the experimental. However, according to recent calculations by Williams[25] the reference velocity of the experiments was about 8 per cent lower than the free-stream velocity. If this difference is taken into account the calculated values for both the pressures and the lift coefficient are in excellent agreement with the measurements. For the same angle of attack calculations were carried out at a higher Reynolds number $Re = 3 \times 10^6$ for which the experimental[22] value of C_L is 1·50. In this case the predicted C_L was found to be 1·52. In Figure 11 the mean velocity vectors are plotted for $Re = 1{\cdot}5 \times 10^6$ (there are only slight differences for the higher $Re = 3 \times 10^6$). A separation bubble is observed near the trailing edge region starting at 80 per cent of the chord length, whereas according to the measurements[24] it was located at a distance of 87 per cent of the chord length from the leading edge. Numerical experiments have shown that when the number of grid nodes was increased from 50×40 to 70×60 the separation point moved towards the trailing edge from 60 to 80 per cent of the chord, whereas the change in the calculated C_p was not significant. A grid-independent solution could not be obtained because a very fine grid resolution is needed at the region of the bubble, which was beyond the capability of the available computer.

The obtained results seem to agree better with the experiments than those by Rhie and Chow[4] and, besides, the convergence rate has been improved drastically. However, although promising, the predictions for the pressure coefficient on the foil surface are not the main objective of the present method, as by a modern viscous–inviscid interaction method[25] the same accuracy (for angles of incidence up to stall) can be obtained at a fraction of the cost. These predictions are only indicative that the selected finite volume scheme and the associated co-ordinate system can be used to solve numerically the complete Reynolds equations, in order to investigate if it is possible to calculate in detail complex turbulent flow fields with existing turbulence models. In this respect, a thorough investigation is still necessary in order to evaluate both the numerical scheme and the turbulence model. First, it is necessary to obtain grid-independent solutions, because applications indicate that computations improve significantly as finer grids are used. The calculated mean velocity profiles and Reynolds stresses will also have to be compared with experiments in order to assess the applicability of the k–ε turbulence model and the associated wall functions (the standard

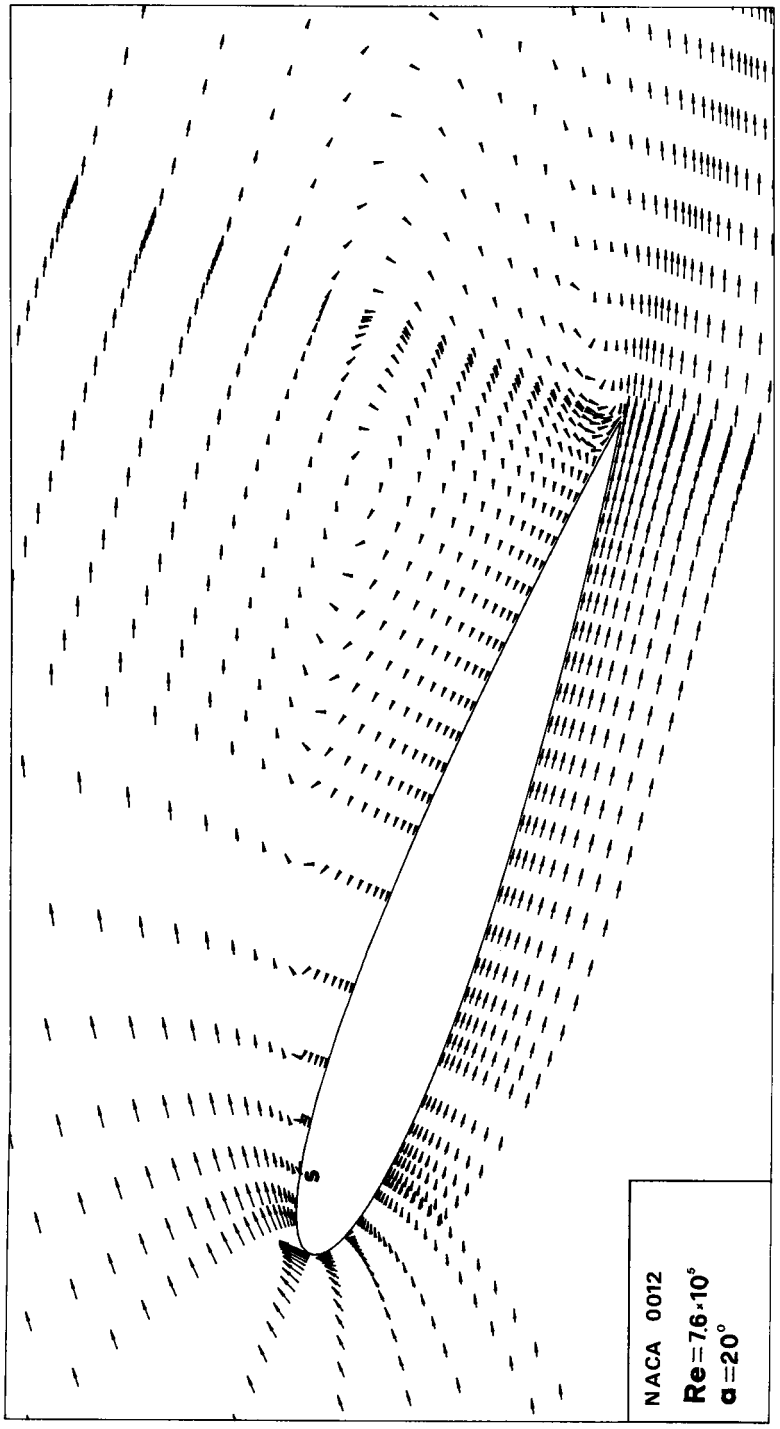

Figure 9. Mean velocity vector plot around the NACA 0012 aerofoil

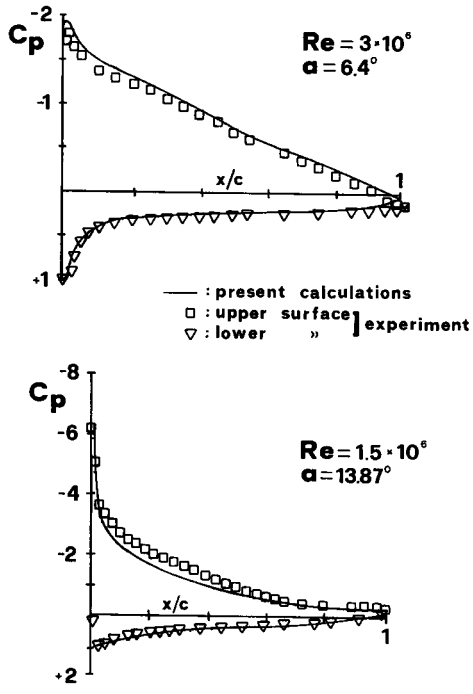

Figure 10. Comparison of pressure distributions around the NACA 4412 aerofoil

wall function method which is based on the logarithmic law (7) neglects the pressure gradient and the curvature terms which are very important around the leading edge). Another problem which has not yet been investigated is the effect of the laminar flow region on the numerical solution. If a laminar separation bubble occurs it will affect the numerical results at least near the leading edge. The determination of the transition point cannot be predicted analytically, but its location may be specified from existing experimental data. It should be noted here that experiments for separated flows are very difficult and measurements always have uncertainties which must kept in mind when comparisons with calculations are made.

CONCLUSIONS

The predictions of the present method for pressure distributions around NACA 0012 and NACA 4412 aerofoils at various angles of incidence seem to be adequate when compared to experiments. Some discrepancies in the calculated pressure coefficients and the estimation of the separation point were observed for angles of attack near stall. However the results improved significantly when finer grids were used. The use of variable underrelaxation factors was found considerably to improve the convergence rate.

Future grid-independent results and the comparisons of the corresponding velocity profiles and Reynolds stresses with experiments are necessary to establish the adequacy of the k–ε turbulence model for the calculation of separated flows around aerofoils.

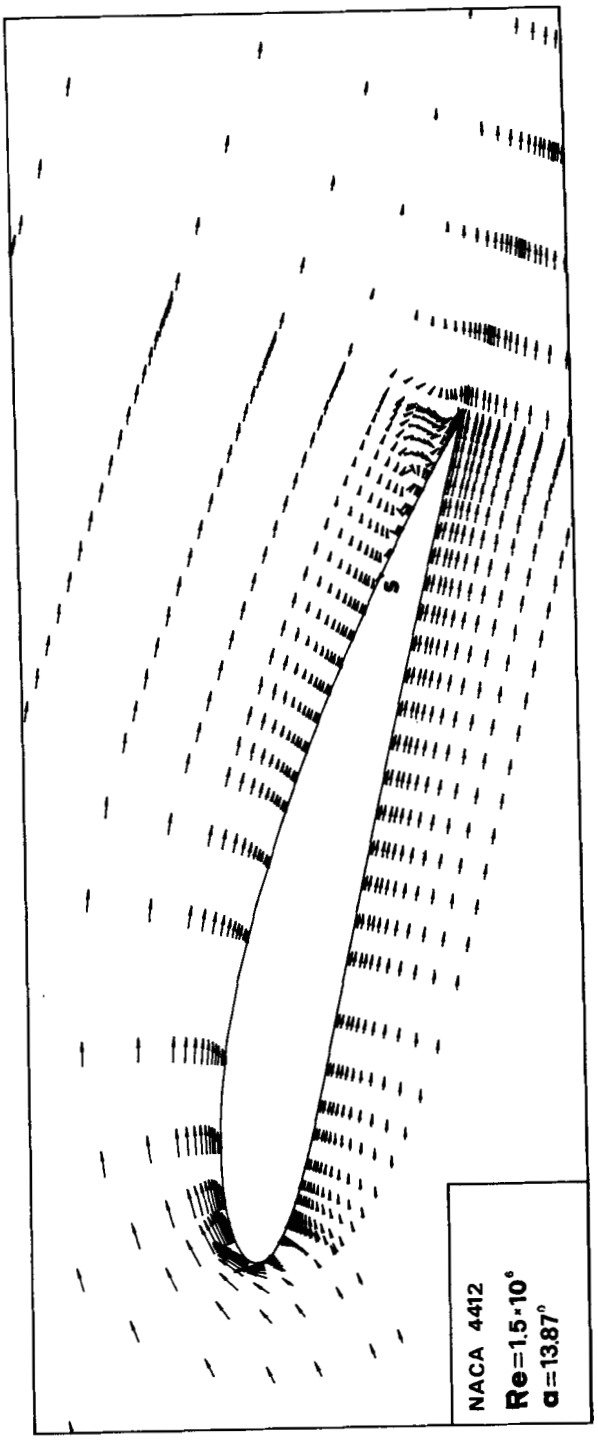

Figure 11. Mean velocity vector plot around the NACA 4412 aerofoil

REFERENCES

1. D. R. Chapman, 'Computational aerodynamics development and outlook', *AIAA Journal*, **17**, 1293–1313 (1979).
2. F. C. Thames, J. F. Thompson and C. Wayne Mastin, 'Numerical solution of the Navier–Stokes equations for arbitrary two dimensional airfoils', *Conference on Aerodynamic Analysis Requiring Advanced Computers*, 1975.
3. J. L. Steger, 'Implicit finite difference simulation of flow about arbitrary two-dimensional geometries', *AIAA Journal*, **16**, 679–689 (1978).
4. C. M. Rhie and W. L. Chow, 'Numerical study of the turbulent flow past an airfoil with trailing edge separation', *AIAA Journal*, **21**, 1525–1532 (1983).
5. B. E. Launder and D. B. Spalding, 'The numerical computation of turbulent flows', *Computer Methods in Applied Mechanics and Engineering*, **3**, 269–289 (1974).
6. W. Rodi, 'Examples of turbulence models for incompressible flows', *AIAA Journal*, **20**, 872–879 (1981).
7. L. P. Hackman, G. D. Raithby and A. B Strong, 'Numerical predictions of flows over backward-facing steps', *Int. j. numer. methods fluids*, **4**, 711–724 (1984).
8. A. D. Gosmann and K. Y. M. Lai, 'Finite difference and other approximations for the transport and Navier–Stokes equations', *IAHR Symposium on* Refined Modelling of Flows, 1982.
9. M. K. Patel, N. C. Markatos and M. Cross, 'A critical evaluation of seven discretization schemes for convection–diffusion equations', *Int. j. numer. methods fluids*, **5**, 225–244 (1985).
10. M. Rosenfeld and M. Wolfshtein, 'Numerical calculation of a laminar two dimensional straight cascade flow', *Computers and Fluids*, **12**, 293–310 (1984).
11. T. Brockett, 'Steady two-dimensional pressure distributions on arbitrary profiles', *David Taylor Model Basin Report 1821*, 1965.
12. A. Dimas, 'Numerical study of the turbulent flow field around a hydrofoil', *Diploma Thesis*, Dept. of N.A.M.E., N.T.U.A., 1985.
13. G. D. Tzabiras, 'Numerical and experimental investigation of the turbulent flow field at the stern of double ship models', *Ph.D. Thesis*, Dept. of N.A.M.E., N.T.U.A., 1984.
14. S. B. Pope, 'The calculation of turbulent recirculating flow in general orthogonal coordinates', *J. Comp. Phys.*, **26**, 197–217 (1978).
15. S. V. Patankar and D. B. Spalding, 'A calculation procedure for heat, mass and momentum transfer in three dimensional parabolic flows', *Int. j. Heat and Mass Transfer*, **15**, 1787–1806 (1972).
16. D. B. Spalding, 'A novel finite-difference formulation for differential expressions involving both first and second derivatives', *Int. j. numer. methods eng.*, **4**, 551–559 (1972).
17. J. Hinze, *Turbulence*, McGraw-Hill, 1977.
18. R. J. Issa, 'Numerical methods for two- and three-dimensional viscous flows', *V.K.I. Lecture Series 1981–5*.
19. P. J. Roache, *Computational Fluid Dynamics*, Hermosa Publishers, 1972.
20. A. W. Neuberger, A. U. Chatwani, E. Eickoff and J. Koopman, 'Selection of relaxation factors for computing steady state turbulent flows', *Proceedings of the Third International Conference on Numerical Methods in Laminar and Turbulent Flow*, 1983.
21. A. Michos, G. Bergeles and N. Athanassiadis, 'Aerodynamic characteristics of NACA 0012 airfoil in relation to wind generators', *Wind Engineering*, **7**, 247–262 (1983).
22. F. W. Riegels, *Airfoil Sections*, Butterworths, London, 1961.
23. J. H. Abbott and A. E. von Doenhoff, *Theory of Wing Sections*, Dover Publications, 1959.
24. D. Coles and A. J. Wadcock, 'Flying-hot-wire study of flow past an NACA 4412 airfoil at maximum lift', *AIAA J.*, **17**, 321–329 (1979).
25. B. R. Williams, 'The prediction of separated flow using a viscous-inviscid interaction method', *Aeronautical Journal*, **89**, 185–197 (1985).